

The Development of a 1D-Transient Simulation Model of a CO₂ Refrigeration System

M Garces de Gois^a & RT Dobson^b

Department of Mechanical Engineering, University of Stellenbosch, Cape Town, South Africa
Private Bag X1, Matieland 7602, South Africa

Refrigeration is a highly essential part of modern day living. The drive for alternative cleaner technologies has renewed interest in designing refrigeration systems using CO₂ as refrigerant. The goal of this project was to develop a numerical transient simulation model of a CO₂ refrigeration cycle containing a capillary tube as expansion device. This simulation model can then be used to design CO₂ refrigerators and provide insight into their operation. In this paper, the transient conservation equations are developed into forms that can be solved on a computer program. An algorithm for solving compressible flow equations is discussed. Lastly the use of the real gas equation of state for CO₂ from Span and Wagner (1996) is discussed and methods are developed to calculate single phase and two-phase properties. It was found that the simulation model predicted evaporator temperature and phase-change processes with reasonable accuracy.

1. Introduction

Refrigeration is a necessity to normal living. Barthel and Götz (2012: 3) state that in 2012 there were an estimated 1.4 billion refrigerators and freezers in use worldwide, with a total annual electricity consumption of 649 TWh.

The phase out of synthetic refrigerants due to their damaging effects to the environment has renewed interest in using CO₂ as refrigerant. The improvement of refrigeration cycles has been the topic of many recent research papers, specifically CO₂ transcritical cycles (Sarkar, 2009; 2010). The urge to design and manufacture CO₂ refrigeration cycles with a higher COP has led to the development of simulation models to obtain a better understanding of the cycle's operating characteristics and to identify areas for improvement. The simulation models are also used to reduce system design time and costs. It is of interest to see how the system reaches steady state operation from standstill starting conditions. This has inspired the development of a transient simulation model of a refrigeration system containing a capillary tube, capable of transient start-up from standstill subcritical conditions through to transcritical operation. The program uses a one-dimensional computational fluid dynamics (1D-CDF) finite volume approach and has

the whole refrigeration circuit, from compressor outlet back to compressor inlet, as the simulation domain. The transient numerical simulation model is capable of both single - and two-phase flow. A CO₂ refrigerator is designed and manufactured, and then used to validate the simulation model developed. The simulation and experimental results are compared and discussed. Finally a discussion of results and recommendations for future work is reported.

2. Conservation Equations

The three conservation equations that govern 1-D fluid flow and heat transfer of a compressible fluid are:

Conservation of mass

$$\frac{\partial \rho}{\partial t} + \frac{\partial}{\partial z}(\rho v_z) = 0 \quad (1)$$

Conservation of energy

$$\frac{\partial(\rho u)}{\partial t} + \frac{\partial}{\partial z}(\rho u v_z) = -P \frac{\partial v_z}{\partial z} + \bar{\tau}_{rz} \frac{\partial(v_z)}{\partial r} + S_u \quad (2)$$

Conservation of momentum

$$\frac{\partial(\rho v_z)}{\partial t} + \frac{\partial}{\partial z}(\rho v_z v_z) = -\frac{\partial P}{\partial z} + \frac{\partial \tau_{rz}}{\partial r} \quad (3)$$

The three conservation equations all have a similar form and can therefore be written for a general variable ϕ as:

$$\frac{\partial(\rho \phi)}{\partial t} + \frac{\partial}{\partial z}(\rho \phi v_z) = S_\phi \quad (4)$$

where $\phi = 1$, $\phi = v_z$, and $\phi = u$ for the respective conservation equations. The implication of this similarity is that these equations can all be solved using the same solving algorithm. To solve these equations in a computer program it is first necessary to develop it into a discretised form. For illustration, the general transport equation, equation (4), is developed into discretised form.

^aE-mail: 15846644@sun.ac.za

^bTel: 27 808 4268; Fax: 27 808 4958; E-mail: rtd@sun.ac.za

Nomenclature

A	Cross-sectional area [m ²]
h	Specific enthalpy [kJ/kg]
P	Pressure [kPa]; Location
\dot{Q}_{ht}	Heat transfer rate [kW]
r	Radial direction [-]
T	Temperature [K]
t	Time [s]
u	Specific internal energy [kJ/kg]
V	Volume [m ³]
v	Velocity [m/s]
z	Axial direction/length [m]

Greek

α	Void fraction [-]
α_v	Relaxation factor for velocity [-]
Δ	Infinitesimal value
ϵ_{isen}	Isentropic efficiency [-]
ϵ_v	Volumetric efficiency [-]
ϕ	General variable
ρ	Density [kg/m ³]
τ_{rz}	Shear stress due to wall friction [kPa]

Subscripts

e	East face
f	Saturated liquid value
g	Saturated vapour value
u	Specific internal energy
w	West face
z	z-direction

Integrating (4) yields:

$$\frac{\partial}{\partial t} \left(\int_{CV} \rho \phi dV \right) + \int_A (\rho \phi v_z) dA = \int_{CV} s_\phi dV$$

and hence the discretised equation:

$$[(\rho \phi)_P - (\rho \phi)_P^o] \frac{\Delta V}{\Delta t} + [\rho v_z A]_e \phi_e - [\rho v_z A]_w \phi_w = \bar{S}_\phi \Delta V$$

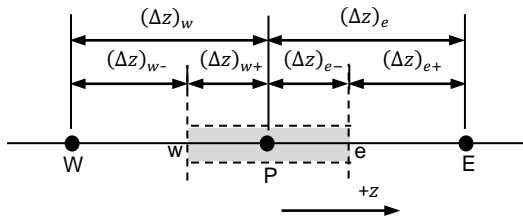


Figure 1: Control volume description

Figure 1 shows the control volume description used to develop discretised equations.

Using an upwind differencing discretisation scheme:

If the flow is in the positive direction $(v_z)_e > 0$, $(v_z)_w > 0$ ($F_e > 0$, $F_w > 0$):

$$\phi_e = \phi_P \text{ and } \phi_w = \phi_W \quad (7)$$

Substitution of the upwind differencing values into the discretised equation yields:

$$[(\rho \phi)_P - (\rho \phi)_P^o] \frac{\Delta V}{\Delta t} + F_e \phi_P - F_w \phi_W = (S_C + S_P \phi_P) \quad (8)$$

Rearranging gives:

$$\left[\rho_P \frac{\Delta V}{\Delta t} + F_e - S_P \right] \phi_P = F_w \phi_W + 0 \cdot \phi_E + \left[\rho_P^o \frac{\Delta V}{\Delta t} \right] \phi_P^o + S_C \quad (9)$$

If the flow is in the negative direction $(v_z)_e < 0$, $(v_z)_w < 0$ ($F_e < 0$, $F_w < 0$):

$$\phi_e = \phi_E \text{ and } \phi_w = \phi_P \quad (10)$$

Substitution of the upwind differencing values into the discretised equation yields:

$$[(\rho \phi)_P - (\rho \phi)_P^o] \frac{\Delta V}{\Delta t} + F_e \phi_E - F_w \phi_P = (S_C + S_P \phi_P) \quad (11)$$

Rearranging gives:

$$\left[\rho_P \frac{\Delta V}{\Delta t} - F_w - S_P \right] \phi_P = 0 \cdot \phi_W - F_e \phi_E + \left[\rho_P^o \frac{\Delta V}{\Delta t} \right] \phi_P^o + S_C \quad (12)$$

(5) Identifying the coefficients of ϕ_P , ϕ_W , and ϕ_E as a_P , a_W , and a_E respectively, equations (9) and (12) can be written in general form as:

$$a_P \phi_P = a_W \phi_W + a_E \phi_E + a_P^o \phi_P^o + S_C \quad (13)$$

(6) where:

$$a_P = a_W + a_E + (F_e - F_w) + (a_P^o) \frac{\rho_P}{\rho_P^o} - S_P$$

$$a_W = \max(F_w, 0) \quad a_E = \max(0, -F_e)$$

$$a_P^o = \rho_P^o \frac{\Delta V}{\Delta t}$$

Discretised equations of the form (13) must be set up at each node in the simulation domain. The discretised equation is modified for boundary control volumes to incorporate boundary conditions.

The equations are now written in the form:

$$-a_W \phi_W + a_P \phi_P - a_E \phi_E = a_P^o \phi_P^o + S_C \quad (14)$$

where ϕ_P is the variable being solved.

The set of equations for the simulation nodes are all written in a matrix starting with the first node's equation in the first row and continuing till the last node's equation in the last row. The resulting matrix has a tri-diagonal form and can then be solved by forward elimination and back-substitution. This algorithm, called the tri-diagonal matrix algorithm (TDMA), can be implemented in a for-loop and is less computationally expensive than direct methods. It requires a number of computations in the order of $\approx 2N$ versus $\approx N^2$ for direct methods, where N is the number of variables being solved. A detailed description of the TDMA algorithm can be obtained in Versteeg and Malalasekera (2007: 213).

3. Determining the Thermodynamic State

The thermodynamic state of the CO₂ in the control volumes is fixed by the density and specific internal energy as determined from the two conservation equations. With reference to the figure below, the CO₂ is two-phase if a point P(ρ, u) lies within the polygon otherwise it is single phase. Vectors containing the saturated values for density and specific internal energy, as shown by the curve, are used together with interpolation to decide the relevant phase.

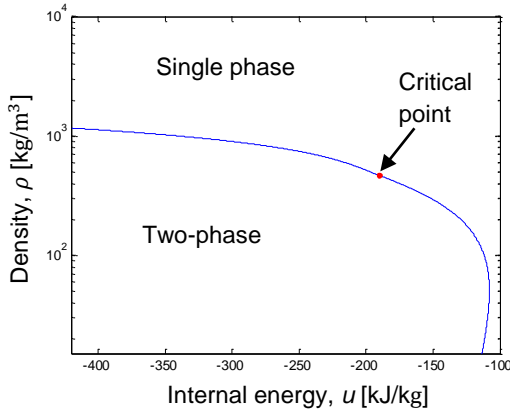


Figure 2: CO₂ phase diagram

Once the phase is known the appropriate function is used to calculate the properties of CO₂ in the control volume. The state properties are calculated by incorporating the Newton-Raphson method with the real gas equation of state for CO₂ from Span and Wagner (1996). This equation of state is a function of

temperature T and density ρ only. Since T is not known it is necessary to iterate from an initial guess, hence the use of the Newton-Raphson method. Figure 3 shows the logic used for determining the properties of CO₂ in the control volumes. The thermal conductivity is calculated by using the equation developed by Scalabrin, Marchi, Finezzo and Span (2006). The dynamic viscosity is calculated by using the equation developed by Fenghour, Wakeham and Vesovic (1998).

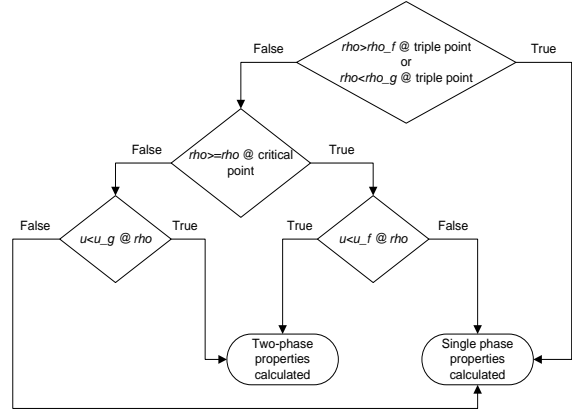


Figure 3: Program logic to determine the properties of CO₂

3.1. Determining Single Phase Properties

Since one of the variables in Span and Wagner's equation is already given, namely the density, it is only required to find the correct temperature that satisfies the given specific internal energy i.e. we may treat u as a function of T only at this fixed density. Therefore, it is wanted that the specific internal energy $u(\rho_x, T)$ calculated from the guessed temperature, or iteratively improved temperature, be equal to the given specific internal energy u_x . Writing the difference between these two in function form gives:

$$f(\rho_x, T) = -u_x + u(\rho_x, T) \quad (15)$$

This has now reduced to a root finding problem which the Newton-Raphson method (Chapra, 2008: 144) is well suited for, especially if a good initial guess for T is available. The error is defined as the absolute value of f .

The new value for T is defined by the Newton-Raphson formula as:

$$T_{i+1} = T - \frac{f(\rho_x, T)}{\frac{\partial f}{\partial T}(\rho_x, T)} \quad (16)$$

where

$$\begin{aligned}\frac{\partial f}{\partial T}(\rho_x, T) &= \frac{\partial}{\partial T}(-u_x + u(\rho_x, T)) \\ &= \frac{\partial}{\partial T}(u(\rho_x, T)) = c_v(\rho_x, T)\end{aligned}\quad (17)$$

Note that u_x is the given specific internal energy and therefore is treated as a constant in the derivation. The values for $u(\rho_x, T)$ and $c_v(\rho_x, T)$ are determined from the equations given by Span and Wagner (1996).

The updated temperature is again used to determine new properties and the whole procedure is repeated until the error reaches a prescribed level. Finally when the error level is reached all thermodynamic properties are updated.

3.2. Determining Two-Phase Properties

Assuming a homogeneous mixture for the two-phase fluid a set of four unknowns emerge. Determining the state from a given density ρ_x and specific internal energy u_x the four unknowns are temperature T , saturated vapour density ρ_g , saturated liquid density ρ_f , and volume fraction α . The temperature and volume fraction at the old time level or previous iteration can be taken as a good initial guess. Equations (3.14) and (3.15) of Span and Wagner (1996) are used to obtain good guesses for ρ_f and ρ_g based on the guessed temperature. Four equations are needed to determine the four unknowns. These equations are given below.

The two-phase internal energy per volume is represented by:

$$\rho_x u_x = \alpha \rho_g u_g + (1 - \alpha) \rho_f u_f \quad (18a)$$

The two-phase flow homogeneous density is represented by:

$$\rho_x = \alpha \rho_g + (1 - \alpha) \rho_f \quad (18b)$$

The vapour and liquid are in equilibrium thus the pressure is equal for both:

$$P_g(\rho_g, T) = P_f(\rho_f, T) \quad (18c)$$

Also equilibrium between vapour and liquid means that the specific Gibbs energy g is the same for both phases:

$$g_g(\rho_g, T) = g_f(\rho_f, T) \quad (18d)$$

The specific Gibbs energy is defined as:

$$g = h - Ts \quad (19)$$

where h is the specific enthalpy, T is the temperature, and s is the specific entropy.

Simultaneously solving the four equations (18a-d) necessitates an efficient method, hence the Newton-Raphson method is again implemented⁵. First the four equations are written in difference form i.e. reduced to a root finding problem.

$$f_1(T, \rho_g, \rho_f, \alpha) = -\rho_x u_x + \alpha \rho_g u_g + (1 - \alpha) \rho_f u_f \quad (20a)$$

$$f_2(\rho_g, \rho_f, \alpha) = -\rho_x + \alpha \rho_g + (1 - \alpha) \rho_f \quad (20b)$$

$$f_3(T, \rho_g, \rho_f) = P_g(\rho_g, T) - P_f(\rho_f, T) \quad (20c)$$

$$f_4(T, \rho_g, \rho_f) = g_g(\rho_g, T) - g_f(\rho_f, T) \quad (20d)$$

Derivatives of these four functions are now developed to use in the Newton-Raphson formula. Note that ρ_x and u_x are the given density and specific internal energy; therefore, they are treated as constants in deriving derivatives of the above functions. Refer to the thesis for derivatives (Garces de Gois, 2016).

The Newton-Raphson method is applied to simultaneously solve the set of equations (20a-d). To use the Newton-Raphson method for a set of equations it is necessary to write the equations in matrix form. The formula remains the same as for solving a single equation in one variable; the only difference is that the derivative is now replaced by a matrix of derivatives.

The vector of unknowns x and the vector of function values f (calculated from equations (20a-d)) are:

$$x = \begin{bmatrix} T \\ \rho_g \\ \rho_f \\ \alpha \end{bmatrix}, \quad f = \begin{bmatrix} f_1 \\ f_2 \\ f_3 \\ f_4 \end{bmatrix}$$

The matrix of derivatives is:

$$J = \begin{bmatrix} \frac{\partial f_1}{\partial T} & \frac{\partial f_1}{\partial \rho_g} & \frac{\partial f_1}{\partial \rho_f} & \frac{\partial f_1}{\partial \alpha} \\ \frac{\partial f_2}{\partial T} & \frac{\partial f_2}{\partial \rho_g} & \frac{\partial f_2}{\partial \rho_f} & \frac{\partial f_2}{\partial \alpha} \\ \frac{\partial f_3}{\partial T} & \frac{\partial f_3}{\partial \rho_g} & \frac{\partial f_3}{\partial \rho_f} & \frac{\partial f_3}{\partial \alpha} \\ \frac{\partial f_4}{\partial T} & \frac{\partial f_4}{\partial \rho_g} & \frac{\partial f_4}{\partial \rho_f} & \frac{\partial f_4}{\partial \alpha} \end{bmatrix}$$

The Newton-Raphson formula for updating the vector x is:

$$x_{i+1} = x_i + J^{-1}f \quad (21)$$

where J^{-1} is the inverse of J .

All derivatives and function values needed in the Newton-Raphson formula are obtained by use of the property calculating script CO2_Property.m (Garces de Gois, 2016).

The error is defined as the maximum absolute value of f . The updated temperature and densities are used again to determine new properties and the whole procedure is repeated until the error reaches a prescribed level. Finally when the error level is reached the vapour fraction is calculated and all homogeneous thermodynamic properties are calculated. The void fraction obtained is later used to calculate the homogeneous viscosity and thermal conductivity. The script file written to determine the two-phase thermodynamic properties is CO2_2Ph_Prop_at_rho_and_u.m (Garces de Gois, 2016).

4. Refrigeration simulation program

A transient simulation program for the basic CO₂ refrigeration cycle, containing a capillary tube as expansion device, is written and will be explained in this section. The one-dimensional finite volume method, as explained in section 2, is used to write the simulation program. The simulation program code may be in the thesis⁶.

4.1. General Model Assumptions

The model assumptions are:

- The refrigerant is pure CO₂ with no oil entrained.
- A homogeneous model is used for two-phase flow.
- No gravity effects are incorporated in the simulation equations since its effects are assumed negligible for such a small household system.
- The compressor operates in a continuous manner with no pauses between suction and expulsion i.e. it sucks and expels gas at the same instant in time. This allows simplification in the simulation model.
- The refrigeration system starts from resting conditions, where the gas in the system is at equilibrium with the surrounding environmental temperature and there is no flow.

4.2. Simulation domain

The simulation domain, consisting of the CO₂ refrigerant flow, is as shown in the figure below. The domain is split into a number of control volumes; the first starting at the compressor outlet and the last is at the compressor inlet. The external heat exchangers are incorporated in the simulation domain through heat transfer source terms in the energy equation.

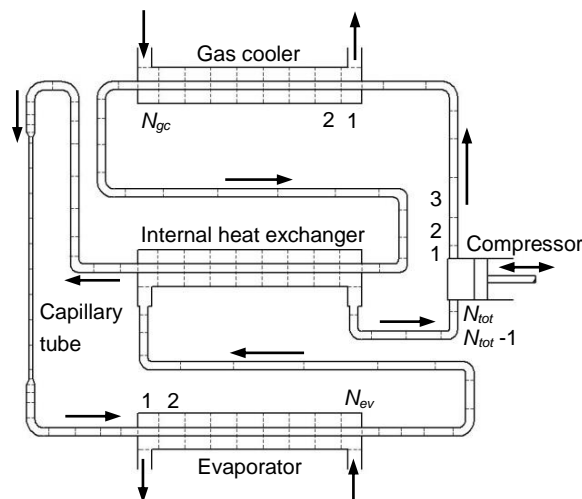


Figure 4: Simulation domain of refrigeration cycle

The initial state of the control volumes are determined from the mass of refrigerant in the system and the initial temperature. The initial temperature of the water in the outer tubes of the gas cooler and evaporator is at ambient temperature of 25 °C. The initial conditions for the CO₂ refrigerant were calculated assuming the system is in equilibrium with its outside environment. The temperature of the CO₂ in the system is thus at environmental temperature:

$$T = T_{Env} = 25\text{ °C} = 298.15\text{ K} \quad (22)$$

The mass of CO₂ charged in the system is:

$$m_{CO_2} = 0.435\text{ kg} \quad (23)$$

The volume of the system is calculated by measuring the length and using the specified inner diameters of the tubes. The properties of the CO₂ can now be calculated based on $\rho = m_{CO_2}/Vol_{system}$ and T . The properties are calculated by a script file called CO2_Prop_at_rho_and_T.m (Garces de Gois, 2016). This function can calculate single phase and two-phase properties. It is determined that the system fluid is two-phase at the initial conditions. To provide starting conditions for the simulation model it was decided to have all the saturated fluid in the last control volumes of the high pressure side and saturated gas in the rest of the control volumes, including the low pressure side. This is a fair

assumption noting that: ⁱ⁾ the highest mass of CO₂ and hence fluid would end up in the high pressure side during and after operation, ⁱⁱ⁾ there is a large enough length/volume of tube on the high pressure side which is lower to the ground than the other tubes, thus enabling gravity to keep the liquid in the high pressure side. The tubing is laid out in this manner to avoid liquid from entering the compressor. ⁱⁱⁱ⁾ Furthermore, the temperature of the low pressure side (with less fluid in it) will go back to the higher environmental temperature when operation stops; thus the fluid inside would end up being saturated gas at the environmental temperature once equilibrium is reached.

The boundary conditions to the simulation domain are as set out below. The inlet water temperature for the outer tubes of the external heat exchangers (gas cooler and evaporator) is 25 °C. The inlet and outlet boundaries of the simulation domain of the CO₂ refrigerant circuit are dependent on the compressor's operating characteristics. Data of the compressor efficiency and speed was not available; hence, some reasonable assumptions are made in this section to develop the simulation model. The boundary conditions are continually updated at the start of each iteration (as needed by the fully implicit temporal scheme used). A continuous compressing model is adopted for the compressor, in which the compressor sucks and expels gas at the same instant in time.

The outlet of the simulation domain is the inlet to the compressor. Therefore:

$$\rho_{in_comp} = \rho(N_{tot}) \quad (24a)$$

$$h_{in_comp} = h(N_{tot}) \quad (24b)$$

$$s_{in_comp} = s(N_{tot}) \quad (24c)$$

The mass flow rate through the compressor is determined by:

$$\dot{m}_{comp} = \rho_{in_comp} Vol_{comp} \frac{N}{60} \varepsilon_v \quad (25)$$

where $Vol_{comp} = 1.75 \times 10^{-6} \text{ m}^3$ is the given compressor displacement volume, $N = 2400$ is the assumed speed of the compressor in rpm, and ε_v is the compressor volumetric efficiency. For the compressor used a value of $\varepsilon_v = 0.954$ is calculated to ensure that equation (25) satisfies the compressor rated mass flow rate as determined from a P - h diagram and the stated performance of the compressor. Also for the simulation model it is assumed that the compressor reaches full speed instantly, at $t = 0$ s.

Since a transient model for the compressor efficiency is not available, it is decided to use a constant efficiency as determined from a steady-state test point. There were however no power usage rated by the compressor manufacturer data; therefore, the compressor efficiency could not be calculated. An isentropic efficiency of $\varepsilon_{isen} = 0.716$ is thus assumed and validated later during experimentation.

The outlet of the compressor is taken to be at the pressure of the first control volume in the simulation domain i.e.:

$$P_{out_comp} = P(1) \quad (26)$$

To determine the state of the CO₂ expelled by the compressor, it is first necessary to calculate the state following an isentropic process. Then an isentropic efficiency is applied to determine the actual state. The state is calculated as follows: For isentropic compression the enthalpy at exit, $h_{out_comp_isen}$, can be determined by the two independent variables at exit already known i.e. from $P = P_{out_comp}$ and $s = s_{in_comp}$. The exit state would be single phase, thus the script file CO2_1Ph_Prop_at_P_and_s.m (Garces de Gois, 2016) is used to determine properties from a given pressure and specific entropy.

The actual enthalpy at the outlet of the compressor can be calculated as:

$$h_{out_comp} = h_{in_comp} + \frac{h_{out_comp_isen} - h_{in_comp}}{\varepsilon_{isen}} \quad (27)$$

All properties at the outlet of the compressor can now be calculated from the pressure and enthalpy, i.e. P_{out_comp} and h_{out_comp} , with the script file CO2_1Ph_Prop_at_P_and_h.m (Garces de Gois, 2016).

The compressor discharge specific internal energy is treated as a source term in the boundary control volume of the energy equation (which is written in the form of specific internal energy) i.e.:

$$S_u = \dot{m}_{comp} u_{out_comp} \quad (28)$$

where S_u is a source of internal energy.

The compressor discharge density is used to calculate the velocity which is treated as an inlet boundary velocity in the momentum equation i.e.:

$$v_z(1) = \frac{\dot{m}_{comp}}{\rho_{out_comp} A_{inlet}} \quad (29)$$

where A_{inlet} is the inlet area of the first control volume.

The outlet boundary velocity of the simulation domain is also defined by the compressor mass flow rate as:

$$v_z(N_{tot} + 1) = \frac{\dot{m}_{comp}}{\rho_{in_comp} A_{outlet}} \quad (30)$$

where A_{outlet} is the outlet area of the last control volume.

4.3. Updating to the New Time-Step

A time-step size of $\Delta t = 0.1$ ms is used in the simulation model, and a convergence level to reach for the three conservation equations of 10^{-8} is set for each time-step. Updating to the new time-step involves assigning the initial (for start-up conditions) or newly obtained density ρ , specific internal energy e and velocity field to variables holding the old values (as these now become the values of the previous time-step). These old values are used in the discretisation of the equations of change as will be seen in section 4.4. A new velocity field guess is established using a projection method which is third order accurate in time. This projection method gives a good guess for the new velocity and hence saves considerable time during simulation. The projection method is developed by using a third order Taylor series expansion (Chapra, 2008: 94) combined with backward finite-difference formulas (Chapra, 2008: 455) for the first, second and third derivatives. The resulting formula for the new velocity guess is as shown here:

$$v_z^{t+\Delta t} = \frac{8}{3}v_z^t - 2.5v_z^{t-\Delta t} + v_z^{t-2\Delta t} - \frac{1}{6}v_z^{t-3\Delta t} \quad (31)$$

where t refers to time and Δt refers to time-step size.

4.4. Discretised equations of change

Figure 5 shows the control volumes used in the discretisation of the three equations of change. The dots represent the nodes where all scalar quantities are calculated and the arrows represent the velocity nodes.

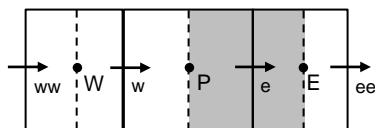


Figure 5: Control volume description

The mass and energy equations are solved on the node centered scalar control volumes i.e. the control volumes surrounding the nodes with capital letter designation. The momentum equation is solved on a staggered grid relative to the scalar control volumes, such as the shaded control volume in the figure. This arrangement is selected since it prevents the

checkerboard pressure field problem encountered in CFD for non-staggered momentum control volumes. Also with this arrangement the calculated pressures are located at the faces of the momentum control volumes; and the calculated velocities can be taken to be at the cell faces of the scalar control volumes. This simplifies the discretisation of these three equations.

The three conservation equations are now developed into a discretised form that is easily capable of being solved by a computer program. A fully implicit temporal discretisation scheme is used. The fully implicit discretisation scheme is unconditionally stable thus larger time-step sizes, than for explicit methods, can be used. A small time-step size is however used to ensure physically realistic results. The fully implicit scheme uses new values only, thus it requires iteration and in most cases under-relaxation is necessary.

The discretisation of the three conservation equations are to follow in the particular order in which it was implemented within the simulation model.

Conservation of Mass

The conservation of mass equation (1) is discretised to give an equation to solve for the new densities based on a velocity or guessed velocity field.

Conservation of mass, repeated here for convenience:

$$\frac{\partial \rho}{\partial t} + \frac{\partial}{\partial z}(\rho v_z) = 0$$

The conservation of mass is first integrated over a control volume and written in terms of finite differences:

$$(\rho_P - \rho_P^o) \frac{\Delta V}{\Delta t} + [\rho v_z A]_e - [\rho v_z A]_w = 0 \quad (32)$$

This expression is now formulated into a form to solve the density field based on a given (or guessed) velocity field:

$$(\rho_P - \rho_P^o) \frac{\Delta V}{\Delta t} + [v_z A]_e \rho_e - [v_z A]_w \rho_w = 0 \quad (33)$$

Define convection values (provides a shortened method of writing the equations) as:

$$F_w = [v_z A]_w \text{ and } F_e = [v_z A]_e \quad (34)$$

where $[v_z A]_w$ is the product of velocity v_z and area A at the western face of the control volume and $[v_z A]_e$ is the product - at the eastern face. Substitution gives:

$$(\rho_P - \rho_P^o) \frac{\Delta V}{\Delta t} + F_e \rho_e - F_w \rho_w = 0 \quad (35)$$

An upwind differencing scheme is selected for the face values of density, due to its robustness when using a small number of control volumes. The development of the final form of the discretised equation for the density follows the same procedure as explained for any general variable ϕ .

The final form is therefore:

$$a_P \rho_P = a_W \rho_W + a_E \rho_E + a_P^o \rho_P^o + S_C \quad (36)$$

where:

$$a_P = a_W + a_E + (F_e - F_w) + a_P^o - S_P$$

$$a_W = \max(F_w, 0) \quad a_E = \max(0, -F_e)$$

$$a_P^o = \frac{\Delta V}{\Delta t}$$

$$S_C = 0 \quad S_P = 0$$

Conservation of Energy

The conservation of energy equation (2) is discretised to give an equation to solve for the new specific internal energy field based on the velocity field already used above and the newly obtained density field.

Conservation of energy, repeated here for convenience:

$$\frac{\partial(\rho u)}{\partial t} + \frac{\partial}{\partial z}(\rho u v_z) = -P \frac{\partial v_z}{\partial z} + \bar{\tau}_{rz} \frac{\partial(v_z)}{\partial r} + S_u$$

The conservation of energy is first integrated over a control volume and written in terms of finite differences:

$$[(\rho u)_P - (\rho u)_P^o] \frac{\Delta V}{\Delta t} + [\rho v_z A]_e u_e - [\rho v_z A]_w u_w \quad (37)$$

$$= -P_P [(Av_z)_e - (Av_z)_w] + \bar{\tau}_{rz} \phi \Delta z \bar{v}_z + \bar{S}_u \Delta V$$

Define convection values as:

$$F_w = [\rho v_z A]_w \text{ and } F_e = [\rho v_z A]_e \quad (38)$$

Substitution and rewriting yields:

$$\left[\rho_P \frac{\Delta V}{\Delta t} \right] u_P + F_e u_e - F_w u_w \quad (39)$$

$$= \left[\rho_P^o \frac{\Delta V}{\Delta t} \right] u_P^o - P_P [(Av_z)_e - (Av_z)_w] + \bar{\tau}_{rz} \phi \Delta z \bar{v}_z + \bar{S}_u \Delta V$$

The source term $\bar{S}_u \Delta V$ is used to incorporate the heat transferred \dot{Q}_{ht} through the tube walls and axial

conduction in the gas. Also to accommodate programming the pressure and shear stress components are included in the source term. Any suitable discretisation method can now be used to represent the face values of specific internal energy. Once again upwind differencing is selected for its robustness and fundamental properties as discussed before. Following the procedure as outlined in section 2.6 gives:

$$a_P u_P = a_W u_W + a_E u_E + a_P^o u_P^o + S_C \quad (40)$$

where:

$$a_P = a_W + a_E + (F_e - F_w) + a_P^o \frac{\rho_P}{\rho_P^o} - S_P$$

$$a_W = \max(F_w, 0) \quad a_E = \max(0, -F_e)$$

$$a_P^o = \rho_P^o \frac{\Delta V}{\Delta t}$$

$$S_C = -P_P [(Av_z)_e - (Av_z)_w] + \bar{\tau}_{rz} \phi \Delta z \bar{v}_z + \dot{Q}_{ht}$$

$$S_P = 0$$

Conservation of Momentum

Before the momentum equation is discretised, the equation of state is used to obtain updated values of all properties, including pressure, based on the newly obtained density - and specific internal energy field.

The conservation of momentum equation (3) is discretised to give an equation to solve for the new velocities based on the newly obtained density field and properties (especially the pressure field).

Conservation of momentum, repeated here for convenience:

$$\frac{\partial(\rho v_z)}{\partial t} + \frac{\partial}{\partial z}(\rho v_z v_z) = -\frac{\partial P}{\partial z} + \frac{\partial \tau_{rz}}{\partial r}$$

Integrating the conservation of momentum over the staggered momentum control volume (shaded control volume in Figure 5) gives:

$$[(\rho v_z)_P - (\rho v_z)_P^o] \frac{\Delta V}{\Delta t} + [\rho v_z A]_e (v_z)_e \quad (41)$$

$$- [\rho v_z A]_w (v_z)_w = -(P_e - P_w) A_P - \bar{\tau}_{rz} \phi \Delta z$$

Define convection values as:

$$F_w = [\rho v_z A]_w \text{ and } F_e = [\rho v_z A]_e \quad (42)$$

Substitute and formulate this expression into a form to solve the velocities:

$$\begin{aligned} \left[\rho_P \frac{\Delta V}{\Delta t} \right] (v_z)_P + F_e(v_z)_e - F_w(v_z)_w & \quad (43) \\ = \left[\rho_P^o \frac{\Delta V}{\Delta t} \right] (v_z)_P^o + (P_w - P_e)A_P - \bar{\tau}_{rz}\delta\Delta z \end{aligned}$$

Using upwind differencing as the discretisation scheme for the face velocities gives:

$$a_P(v_z)_P = a_W(v_z)_W + a_E(v_z)_E + a_P^o(v_z)_P^o + S_C \quad (44)$$

where:

$$a_P = a_W + a_E + (F_e - F_w) + a_P^o \frac{\rho_P}{\rho_P^o} - S_P$$

$$a_W = \max(F_w, 0) \quad a_E = \max(0, -F_e)$$

$$a_P^o = \rho_P^o \frac{\Delta V}{\Delta t}$$

$$S_C = (P_w - P_e)A_P - \bar{\tau}_{rz}\delta\Delta z$$

$$S_P = 0$$

4.5. Algorithm for Simulating Refrigeration Cycle

The flow is compressible, therefore the usual pressure based algorithms such as SIMPLE (Semi-Implicit Method for Pressure-Linked Equations) are not well suited to solving the flow equations. There is a strong link between density and pressure in compressible flows. Figure 6 shows the density-based algorithm to solve the conservation equations for each time-step. The simulation starts with the initial conditions as described in section 4.2. The boundary conditions as set out in section 4.2 are calculated at the start of each iteration (step 1). Each time-step is solved in a similar fashion as with steady-state problems. To start the simulation of the current time-step a velocity field for the scalar control volume faces is guessed or taken as zero for the first time-step. With the guessed velocity field the conservation of mass equation is discretised to form an equation to solve for the new density field (step 2). The velocities with the newly obtained densities are then used in the discretisation of the energy equation to form an equation to solve for the new specific internal energy field (step 3).

The newly obtained density and specific internal energy are now used in the equation of state to determine the new pressures and all other properties (step 4). The new pressures, densities and other variables are then used in the discretisation of the momentum equation to form an equation to solve for the new velocity field (step 5). Finally the residuals of each conservation equation are compared to a certain convergence level. If convergence is reached then the iteration stops and the solution is advanced to a new

time-step, else it will re-iterate with the new velocity. A relaxation factor, α_v , is applied to the velocity field in order to facilitate convergence where the new guess for velocity v^* is defined as:

$$v^* = (1 - \alpha_v)v^* + \alpha_v v \quad (45)$$

where v^* on the right hand side is the previously guessed/used velocity and v is the newly calculated velocity. A relaxation factor of $\alpha_v = 0.050$ proved to produce stable results from initial start-up till steady-state. The script file `Iterate_UD_density_based.m`, performs the function of Figure 6 (Garces de Gois, 2016).

The convergence indicator, of how well the current variable satisfies the new coefficients, is determined by the use of a normalised global residual⁴ which is defined as:

$$norm_{Global_{residual}} = \frac{\sum(abs(residual))}{\sum(abs(norm_factor))} \quad (46)$$

where the *residual* is defined as the difference between left and right hand sides of the discretised equation for a node:

$$residual = a_P \phi_P - (a_W \phi_W + a_E \phi_E + a_P^o \phi_P^o + S_C) \quad (47)$$

and the normalisation factor, *norm_factor*, is the left hand side of the discretised equation, $a_P \phi_P$. Convergence is reached when the normalised global residuals reach a level of 10^{-8} .

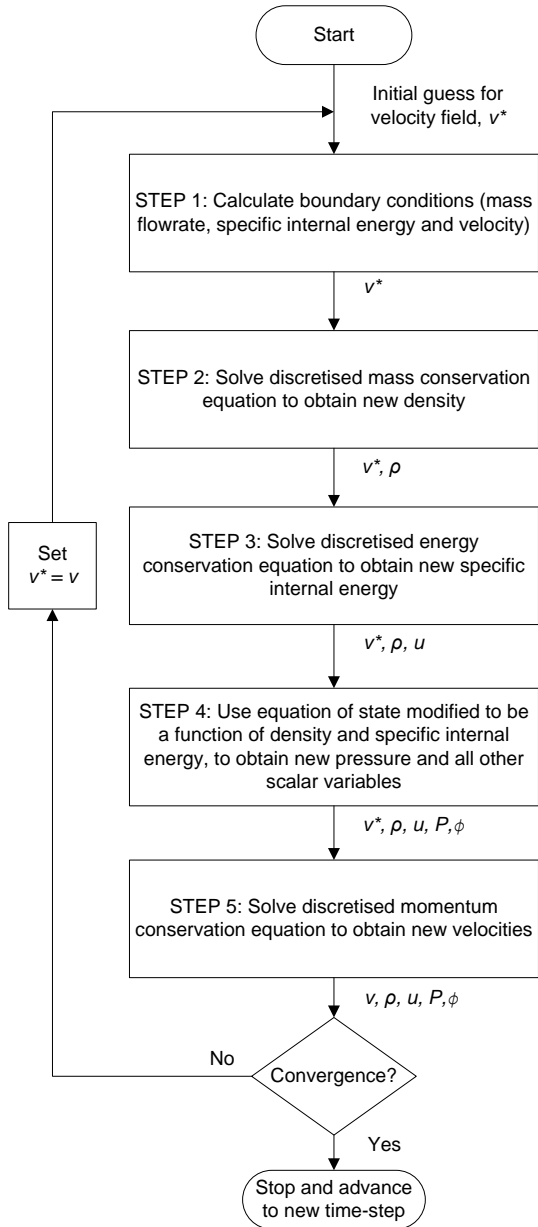


Figure 6: Density-based algorithm for solving compressible flow

5. Refrigerator Design

A small refrigerator is built to provide experimental test results in order to compare and validate the simulation model developed. The test refrigerator built is as shown in Figure 7.

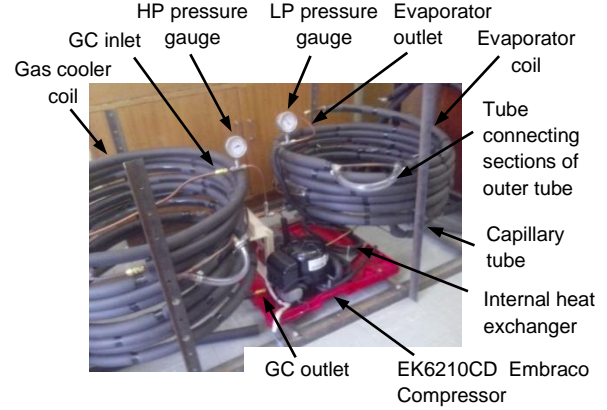


Figure 7: Refrigerator built

The compressor used is the Embraco EK6210CD (Embraco, [S.a]). This compressor has a rated cooling load of 700 W at an evaporation temperature of $-10\text{ }^{\circ}\text{C}$ and uses CO_2 as refrigerant. The compressor specifications state that the maximum CO_2 refrigerant allowed in a system is 500 g; and the maximum density in the high side (in the event of capillary tube blockage) should not exceed 0.65 g/cm^3 . With this in mind the high pressure side was designed. A CO_2 mass of 435 g is selected to use with the system.

Based on the mass of refrigerant used, the high side volume must be larger than:

$$V_{\text{HP Lower limit}} = \frac{\text{Mass used}}{\text{Density limit}} = \frac{435\text{ g}}{0.65\frac{\text{g}}{\text{cm}^3}} \quad (48)$$

$$= 669.231\text{ cm}^3$$

Thick walled copper tubes are used for the refrigerator, in order to withstand the high pressures encountered in a CO_2 refrigerant refrigerator. The details of the high side tubes are shown in the table below.

Table 1: Tube details of the high pressure side

Tubes used for the high pressure side	Length, outer diameter, thickness, pressure rating	Inner volume (cm ³)
Connecting tube between compressor and gas cooler (L_{comp_gc})	2.15 m, 6.35 mm (1/4"), 0.91 mm, 119.9 bar	34.652
Gas cooler tube (L_{gc})	19.7 m, 8 mm, 0.9 mm, 93.9 bar	594.757
Connecting tube between gas cooler and internal heat exchanger (L_{gc_IHx})	1 m, 6.35 mm, 0.91 mm, 119.9 bar	16.117
Internal heat exchanger inner tube (L_{IHx})	2.5 m, 4.76 mm (3/16"), 0.61 mm, 105.9 bar	24.606
Connecting tube between inner tube of IHX and capillary tube (L_{IHx_ct})	0.45 m, 4.76 mm (3/16"), 0.61 mm, 105.9 bar	4.429
Total internal volume		674.558

The capillary tube was designed to operate at the rated conditions of the compressor using a steady-state capillary tube simulation model (Garces de Gois, 2016).

The volume of the low pressure side depends on the evaporator temperature wanted and the rated cooling load of the compressor. These are a -10 °C evaporation temperature and a 700 W cooling load. The transient simulation program developed is used to determine the low pressure side volume by successively trying different volumes (tube lengths) until the one selected suits the conditions mentioned above. Table 2 shows the tube details of the low side.

Table 2: Tube details of the low pressure side

Tubes used for the low pressure side	Length, outer diameter, thickness, pressure rating	Inner volume (cm ³)
Evaporator tube (L_{ev})	12.9 m, 8 mm, 0.9 mm, 93.9 bar	389.460
Connecting tube between evaporator and internal heat exchanger (L_{ev_IHx})	0.93 m, 6.35 mm (1/4"), 0.91 mm, 119.9 bar	14.989
Internal heat exchanger outer tube (L_{IHx})	2.5 m, 9.53 mm (3/8"), 0.91 mm, 79.6 bar	72.230
Connecting tube between internal heat exchanger outer tube and compressor (L_{IHx_comp})	0.35 m, 6.35 mm (1/4"), 0.91 mm, 119.9 bar	5.641
Total internal volume		482.320

The external heat exchanger designs depend on the heat transfer rate needed and the convection coefficients of the fluids exchanging the heat. For this project tube-in-tube heat exchangers, with water in the outer tubes, are used for the gas cooler and the evaporator. Water has a high convection heat transfer coefficient and a high specific heat relative to air; therefore, it can absorb/reject more heat per mass and at a faster rate than air. Also it is easy to control and measure its temperature and mass flow rate; therefore it provides for a reliable method for validation of heat transferred during experimentation.

Both evaporator and gas cooler are over designed to handle higher heat transfer rates if needed; thus providing variable operating conditions for the refrigeration system. The water inlet temperature and mass flow rate to the heat exchangers can be varied; also sections of the heat exchangers can be included or excluded in order to accomplish different cooling/heating loads. The refrigerator built thus serves as a good experimental unit, capable of being tested thoroughly at different operating conditions. Table 3 shows the details of the gas cooler - and evaporator outer tubes.

Table 3: Details of the outer tubes of the heat exchangers

Tube lengths for the external heat exchanger outer tubes	Length, outer diameter of inner tube, outer diameter of outer tube, thickness of outer tube, pressure rating of outer tube	Inner volume (cm ³)
Gas cooler heat exchanger outer tube	14 m, 8 mm, 15.88 mm (5/8"), 0.71 mm, 34.40 bar	1595.365
Evaporator heat exchanger outer tube	12 m, 8 mm, 15.88 mm (5/8"), 0.71 mm, 34.40 bar	1367.456

6. Simulation Setup

The simulation setup follows the experimental setup for a 25 °C initial temperature and water inlet temperature to the external heat exchangers. The 14 m gas cooler cooling section starts at $z = 2.17$ m. The initial state of the simulation domain is discussed first, followed by the boundary conditions and external heat exchangers, then a grid independence study is shown, and finally the simulation geometry properties are discussed.

6.1. Initial State of the Simulation Domain

The initial state of the simulation domain can be seen in Figure 8. Note the saturated fluid at the end of the high pressure side and the saturated vapour in the rest of the system as seen in the figure below, following the assumption mentioned in section 4.2. The velocity of the simulation domain is zero at initial conditions, the temperature is 25 °C and the pressure is 6434 kPa.

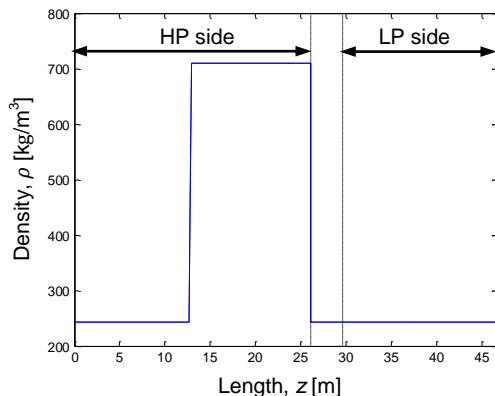


Figure 8: Initial density distribution of the simulation domain

6.2. Boundary Conditions and External Heat Exchangers

The boundary conditions, enforced by the compressor, for the simulation domain are as discussed in section 4.2; with a step-input compressor speed at $t = 0$ s of $N = 2400$ rpm, a constant compressor volumetric efficiency of 0.954 and a constant isentropic efficiency of 0.716.

The external heat exchangers (gas cooler and evaporator) contain water flowing in the outer tubes at a mass flow rate of 0.050 kg/s, in a counter flow direction in relation to the CO₂ refrigerant flow, and at an inlet temperature of 25 °C.

6.3. Grid Independence

A grid independence study is done, as shown here in Figure 9, for the pressure distribution at 150 ms simulation time. It was decided to use the pressure distribution as an indication of grid independence, since all fluid properties are dependent mainly on the operating pressure in the system. The pressure distribution for the different grid sizes show that further grid refinement produces no remarkable difference; thus grid independence has been achieved. Based on this study and in the interest of producing results that are reasonably accurate, in the least amount of time, it was elected to use a grid size of $N_{tot} = 1390$ i.e. use 1390 control volumes.

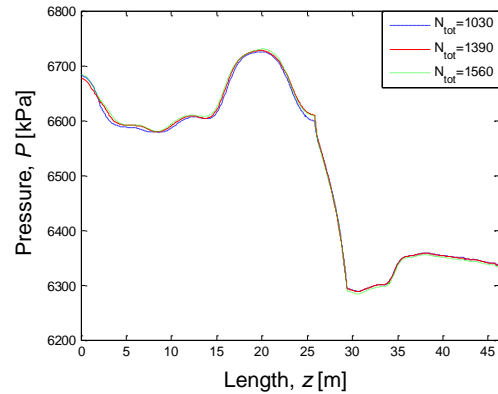


Figure 9: Pressure distribution at 150 ms for grid independence study

6.4. Simulation Domain Geometry Properties

From the grid independence study it was chosen to use a total number of 1390 control volumes for the simulation domain. The number of control volumes are 400, 120, 230, and 300 for the gas cooler, internal heat exchanger, capillary tube and evaporator, respectively.

Figure 10 shows the control volume lengths for the different sections. A stretch ratio is applied to the different tube sections i.e. variable control volume lengths are used. The minimum control volume length is decided as 0.015 m, which is due to transition pieces used between tube sections. The stretch ratio is kept close to a value of one in order to have a good aspect ratio from one control volume to the next, thus ensuring that lengths are kept as short as possible. Furthermore, the stretch ratio for each section is defined such that the end control volumes are close to the 15 mm minimum length in order to ensure a smooth transition to the next tube section.

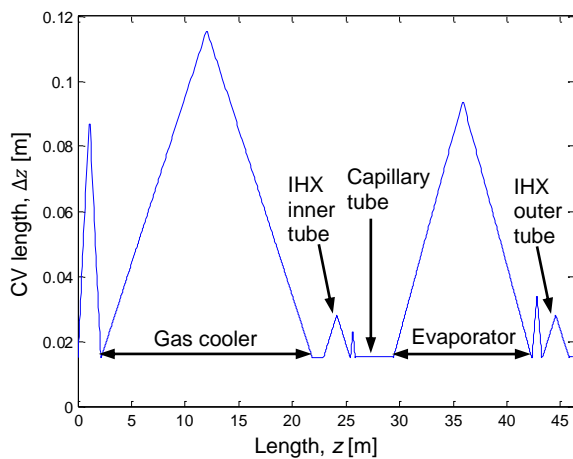


Figure 10: Control volume length distribution

7. Simulation Results

The transient and steady-state results of the simulation, with setup as discussed in section 6, are shown in this section. These results were used to confirm the design; hence, giving the go-ahead to manufacture the refrigerator.

7.1. Transient Simulation Results

The transient simulation results, shown in this section, provide valuable insight as to how a refrigeration system operates. Figure 11 shows the transient development of pressure in the CO₂ refrigeration system from compressor outlet at 0 m to compressor inlet at 46.6 m. Notice how the pressure wave travels through the simulation domain at the speed of sound (190-275 m/s for saturated gas to saturated fluid at the initial conditions) as expected. The capillary tube located between high pressure (HP) and low pressure (LP) side provides a “barrier” to increase the pressure difference as needed.

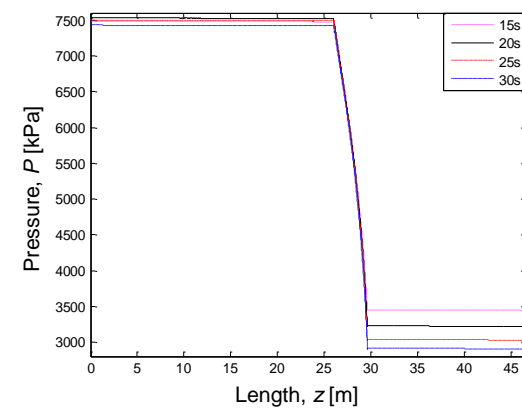
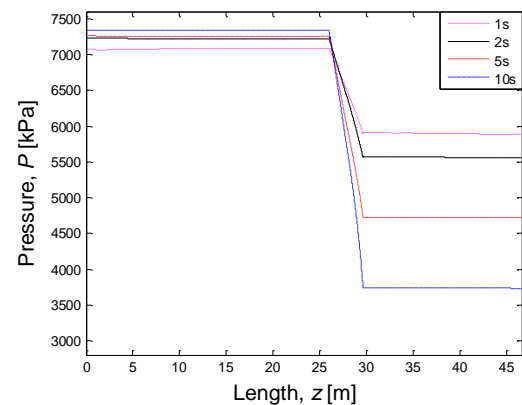
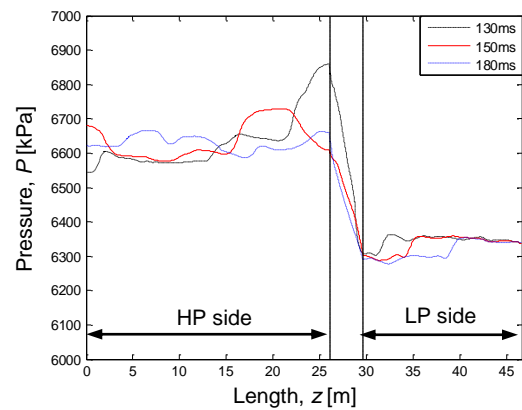
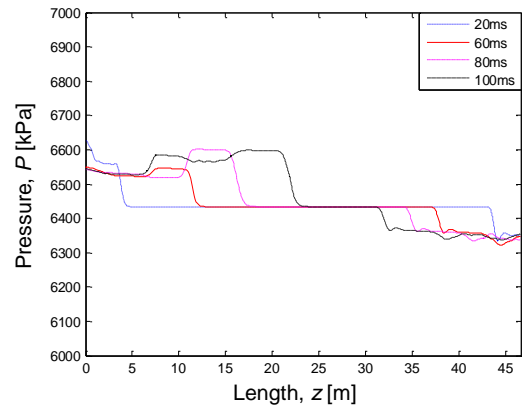


Figure 11: Transient pressure development

Figure 12 shows the transient development of temperature in the refrigeration system. Notice the constant temperature section at 30 m as seen in the

bottom graph. This is the first part of the evaporator, where heat addition causes phase change, at constant temperature, to the gas phase and subsequent heat addition causes a temperature rise. The middle graph is labelled to explain the temperature changes occurring. Note the initial distribution of liquid and vapour as shown previously in Figure 8. The vapour temperature increases much faster with increasing pressure than the liquid.

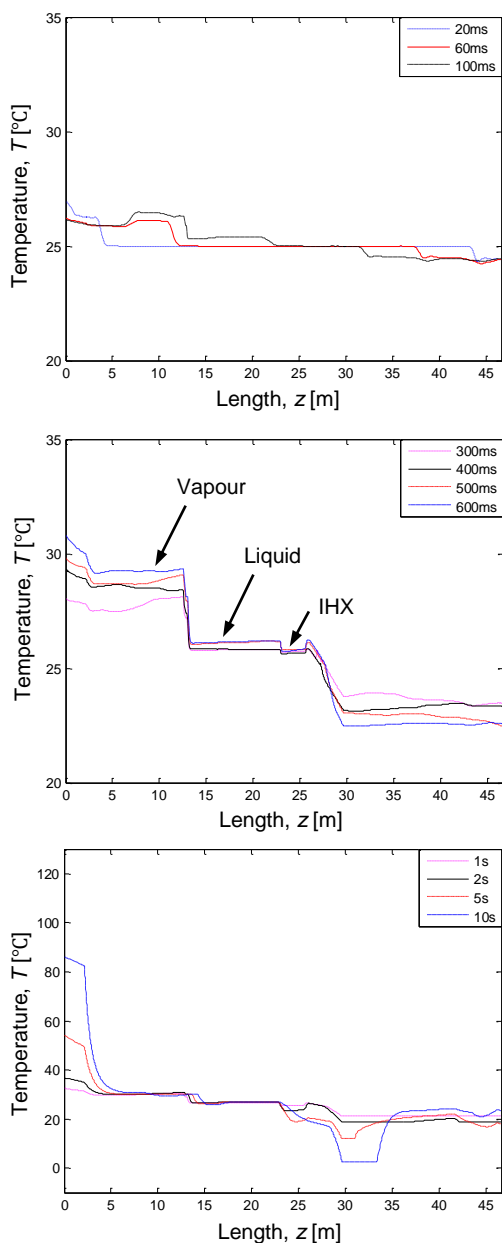


Figure 12: Transient temperature development

Figure 13 shows the transient velocity development. Note the higher velocity encountered in the connecting tubes and the substantially higher velocity in the capillary tube, due to their smaller inner diameters. The higher velocity towards the end of the capillary tube is due to the decreasing density with length through the capillary tube.

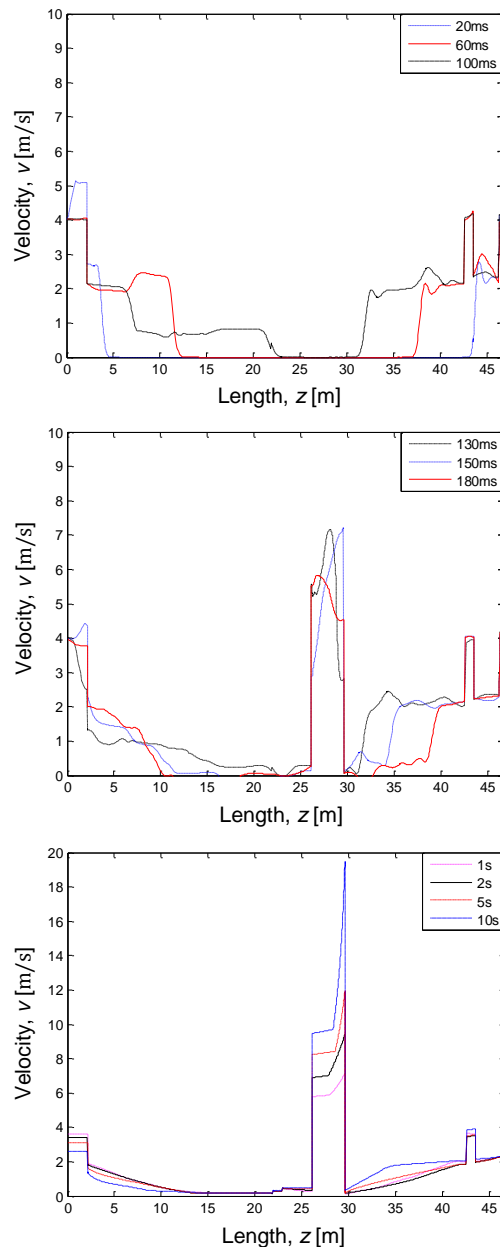


Figure 13: Transient velocity development

Figure 14-(a) shows the transient mass flow rate development throughout the simulation domain. The straight line seen at 70 s is a confirmation that steady-state has been achieved throughout the simulation domain. Figure 14-(b) shows the development of mass flow rate of the compressor over time (serves as boundary condition to the simulation domain). It shows that the compressor has a high mass flow rate at the start of the simulation and gradually decreases until a steady mass flow rate is achieved. The steady-state mass flow rate is 3.66 g/s at a steady-state cooling load of 772 W as shown in Figure 15-(a). This steady mass flow rate is close to the 3.54 g/s initially obtained from the compressor manufacturer operating conditions, with a rated cooling load of 700 W (Garces de Gois, 2016).

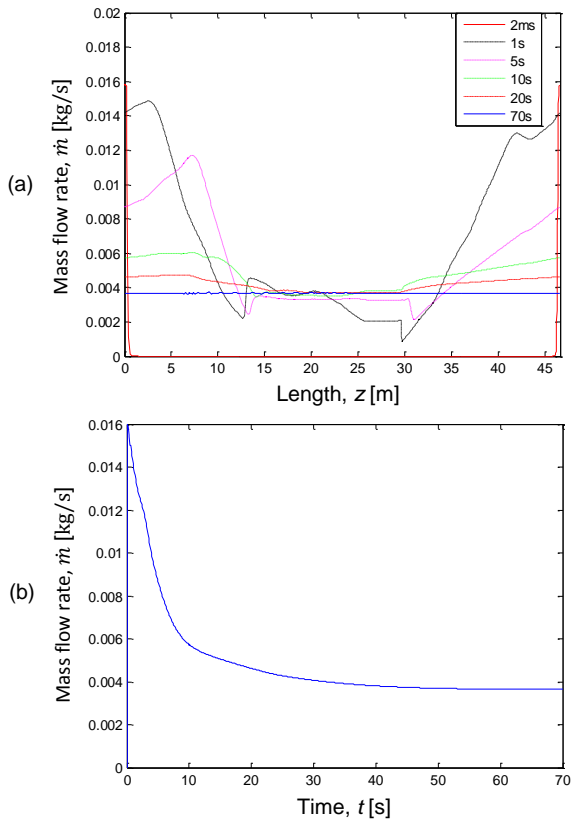


Figure 14: Transient mass flow rate development of: (a) simulation domain, (b) compressor

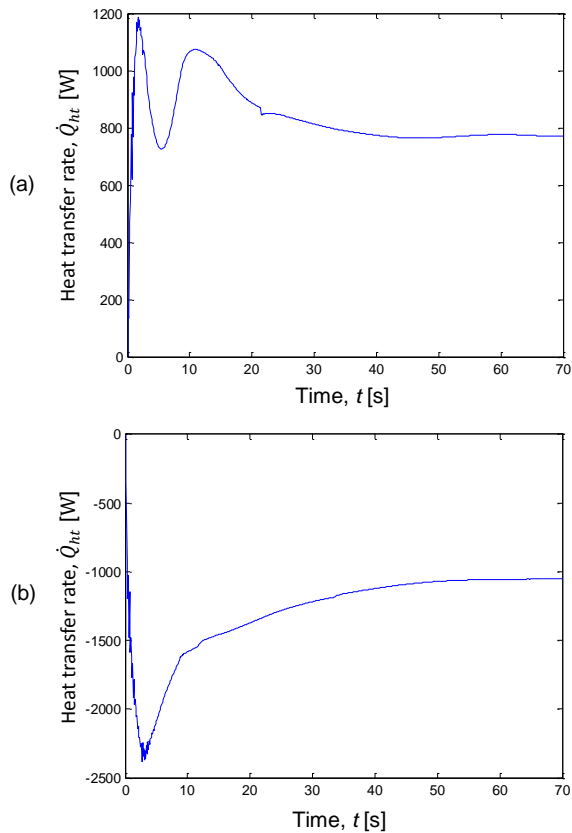


Figure 15: Transient development of: (a) evaporator heat absorption rate, (b) gas cooler heat rejection rate

A higher cooling load requires a higher mass flow rate; thus, the model gives results that are expected. The gas cooler steady-state heat rejection rate is 1050 W, as shown in Figure 15-(b). This result seems reasonably as well, since the heat rejected by the gas cooler is the sum of evaporator cooling load and the compressor power input to the gas. Based on these two values the compressor power input to the gas is 278 W. Figure 16 shows the transient development of vapour quality in the simulation domain.

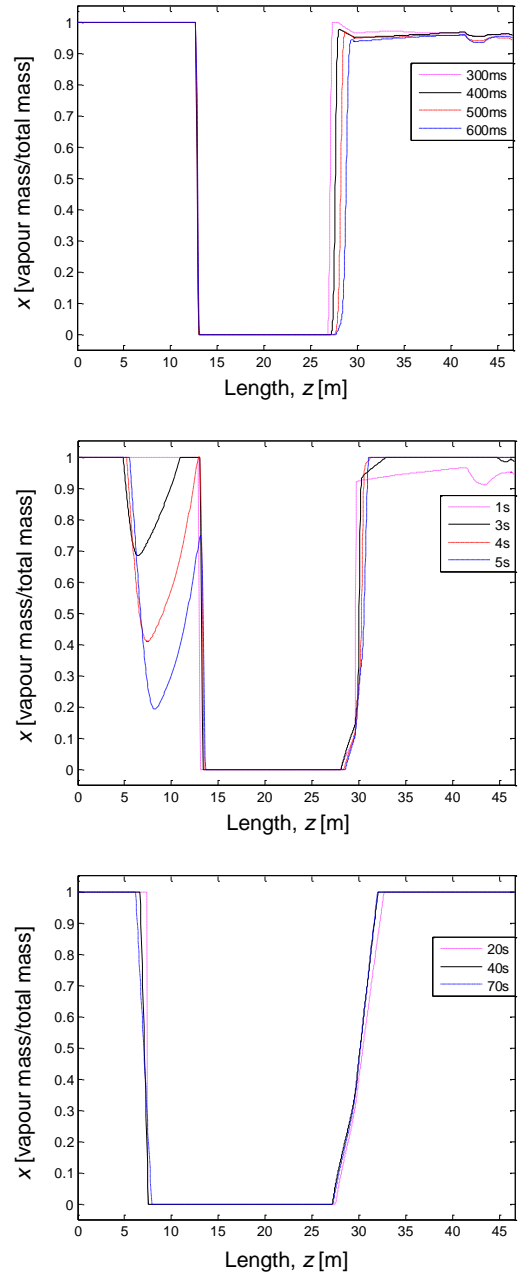


Figure 16: Transient vapour quality development

The figures above shows that for the first few seconds the vapour quality at the simulation outlet (compressor suction) becomes slightly two-phase. The simulation starts with saturated gas in the low pressure side; as soon as some mass is removed by the compressor the

fluid becomes slightly two-phase. However, the flow quickly becomes single phase again, before 4 s, since the heat transferred by the evaporator and by the internal heat exchanger now starts to become significant enough to ensure that the fluid is heated past the saturation point. On the HP side it is seen that the flow transitions from gas to liquid between 1 and 10 s. This transition is caused by the heat rejected by the gas cooler i.e. the gas turns to two-phase and then to liquid with the loss of energy. The transition seen from liquid to gas at about 30 m shows the operation of the capillary tube and the heat addition in the first part of the evaporator.

7.2. Steady-State Results

The steady-state results achieved by the simulation are shown in Figure 16.

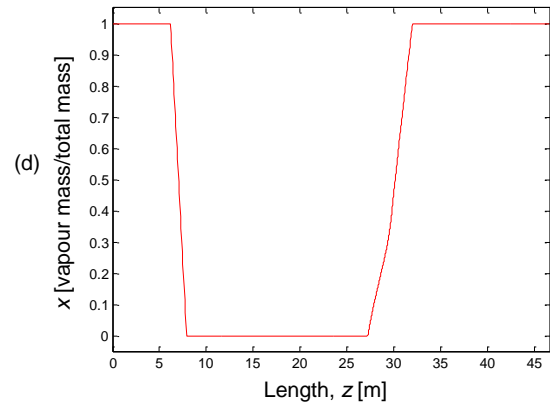
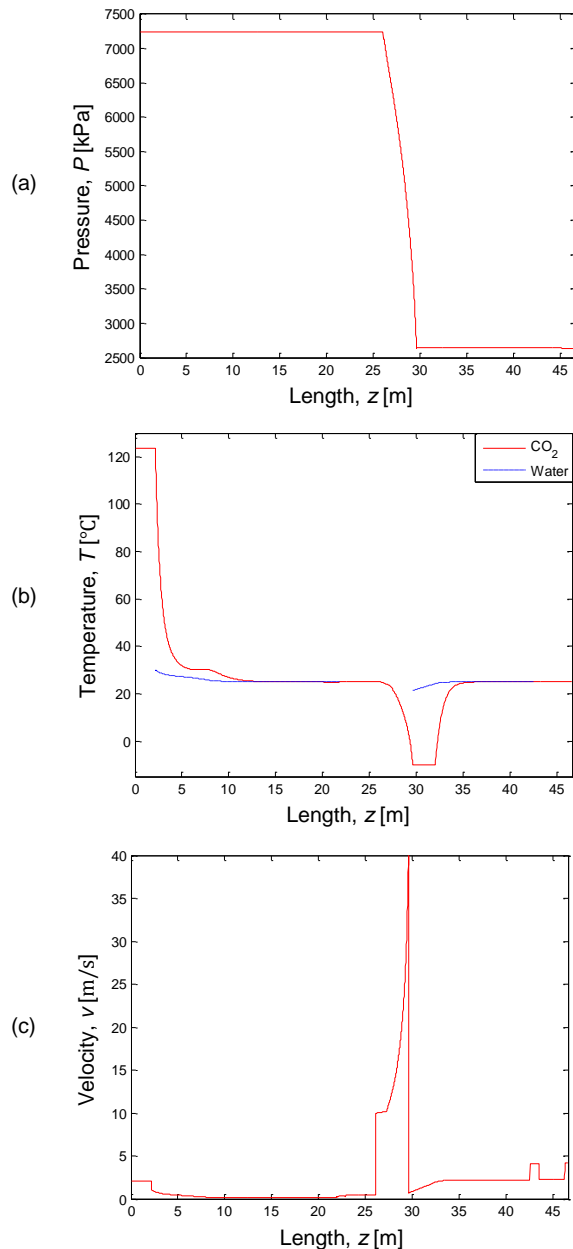


Figure 17: Steady-state results for the distribution of: (a) pressure, (b) temperature, (c) velocity, (d) vapour quality

The dashed lines shown in Figure 16-(b) show the temperature of the water in the outer tubes of the external heat exchangers (evaporator and gas cooler). The flow of water is from right to left in the figure. The flow of CO₂ is from left to right, thus the external heat exchangers are set up in a counter flow arrangement. The increase in water temperature in the gas cooler is 5.04 °C; and the decrease in water temperature in the evaporator is 3.70 °C.

The transient simulation model predicts a steady-state pressure drop for the HP side of 6 kPa, the pressure drop through the capillary tube is 4409 kPa and the pressure drop for the LP side is 10 kPa. Hence, one can approximate the LP and HP side as a constant pressure process.

8. Experimental versus Simulation Results

In this section the experimental results are compared to the simulation results. The experimental results used are from one of three experiments done at the same conditions to confirm repeatability. The experimental temperatures were measured by tightly tying the thermocouples to the outside of the copper tubes. The simulation temperatures refer to the temperature of the CO₂ flowing inside the tubes.

The simulation results shown in section 8, and this section, are for the case where the initial conditions are 25 °C, water inlet temperature to the heat exchangers are also 25 °C, the water mass flow rate is 0.050 kg/s, and the cooling section of the gas cooler is 14 m long and starts at a distance z = 2.17 m from the simulation domain inlet. The experimental refrigerator was however built with the gas cooler cooling section starting at z = 7.73 m. It is expected that this discrepancy would not cause much of a difference to

the actual operation of the refrigerator. Furthermore, it was not possible to obtain the wanted 0.050 kg/s water mass flow rate for the experiment; consequently, the average mass flow rate measured for the evaporator and gas cooler outer tubes are 0.045548 kg/s.

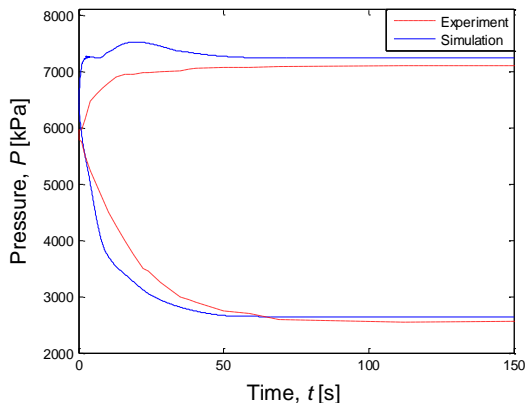


Figure 18: Comparison of pressure development

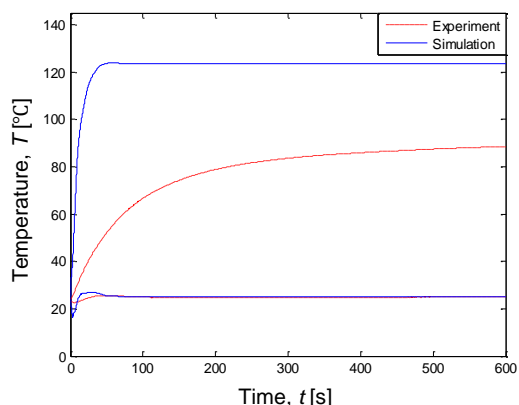


Figure 19: Comparison of compressor inlet and outlet temperature

development predicted by the simulation and what was recorded in the experiment. The initial pressures of the experiment and simulation are 5900 kPa and 6434 kPa, respectively. The saturation temperature for CO₂ at 5900 kPa is 21.25 °C. This confirms the initial suspicion that the CO₂ (low conductivity) has not yet reached the new experimental ambient temperature from the previous night's colder temperature. Furthermore, from the figure it is seen that the simulation develops relatively faster than the experiment does, but reaches a steady-state that is relatively close to the experiment. The quick response of pressure is due to the use of a constant isentropic efficiency from start-up and the assumption that the compressor is at full speed from $t = 0$ s. The water being as close as possible to the compressor outlet dampens the pressure by absorbing heat, thus ensuring that the pressure doesn't reach hazardous high levels. The compressor is a hermetically sealed unit that is intentionally cooled during operation; thus,

cooling the gas while it is being compressed. The efficiency would thus be a changing function that is dependent on the transient operating conditions and cooling. It is thus recommended to rather use an isothermal (non-adiabatic) efficiency model for the compressor (Cengel & Boles, 2007: 379). The use of an isentropic model results in more energy input to the gas than is encountered in actual operation. Hence, the higher compressor outlet temperatures predicted, as seen in Figure 19. The compressor inlet temperature trend and steady-state agrees well with the experiment.

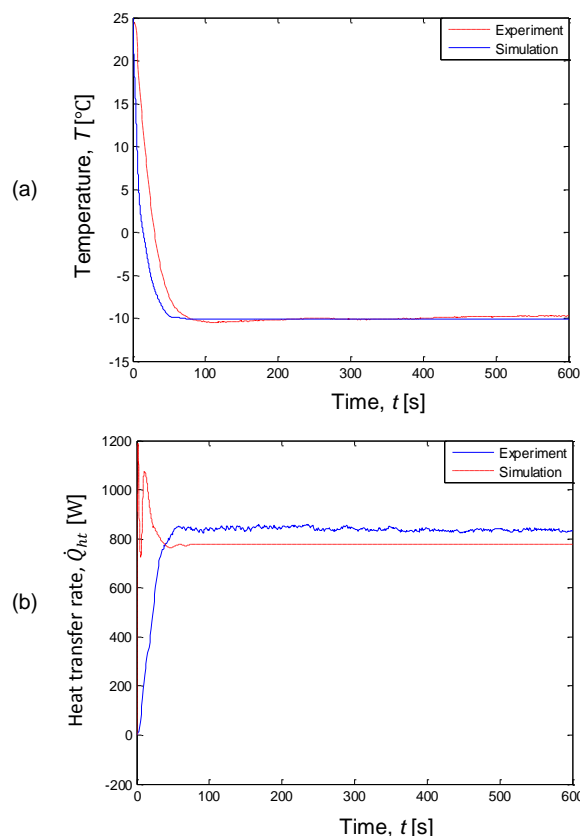


Figure 20: Comparison of evaporator (a) inlet temperature, (b) cooling load

Figure 20 shows a comparison of the evaporator temperature and cooling load for the simulation model versus the experiment. It is seen that the simulation predicts a faster temperature drop than measured in the experiment. The simulation predicts a steady-state evaporator temperature of -10.05 °C, which agrees closely with the experimental result of -9.75 °C. The design goal of the experimental refrigerator was an evaporator temperature of -10 °C for a cooling load of 700 W, as given by the rated performance of the EK6210CD compressor used. The steady-state cooling load measured in the experiment is 830 W (with a water temperature decrease of 4.36 °C), while the simulation predicts a steady-state cooling load of 772 W (with a water temperature decrease of 3.70 °C (note: higher mass flow rate for simulation)). This is

relatively close, thus the simulation model correlates well to the actual system.

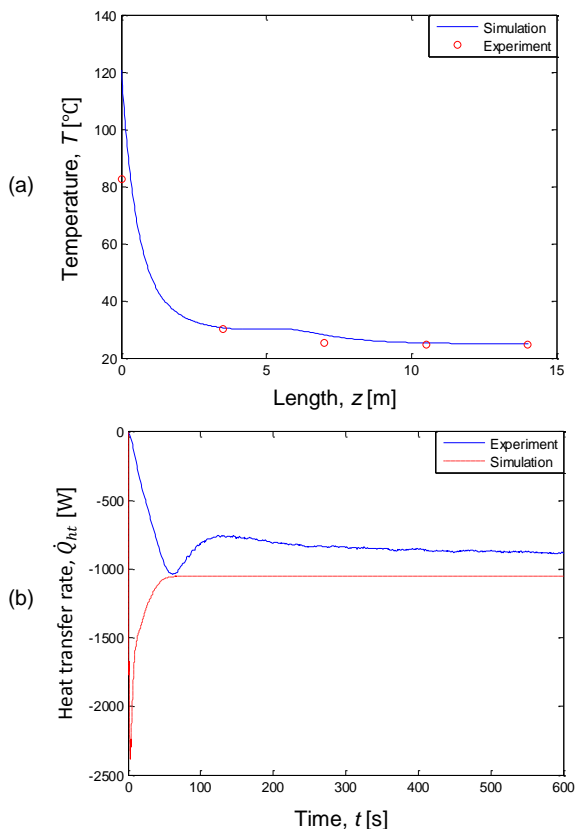


Figure 21: Comparison of gas cooler cooling section (a) steady-state temperature distribution, (b) heat transfer rate

Figure 21-(a) shows a comparison of the gas cooler cooling section temperature distribution. The experimental results are from five thermocouples placed, with a spacing of 3.5 m from each other, along the section length. The inlet to the gas cooler predicted by the simulation is higher than in the experiment. The temperature distribution trend agrees well with the experiment, confirming that most of the cooling occurs in the first 7 m of the cooling section. The gas cooler heat rejection rate development through time is shown in Figure 21-(b). The simulation predicts a higher heat transfer rate at the start, but does follow the trend recorded in the experiment. The steady-state temperature increase of the water measured in the experiment is 4.65 °C and the corresponding heat loss rate is 885 W. The simulation predicted steady-state values for water temperature increase and heat loss rate of 5.04 °C and 1050 W, respectively. The higher heat loss predicted by the simulation is due to the use of an isentropic efficiency model for the compressor, which gives a higher compressor outlet temperature. Thus, more heat will now be extracted by the 25 °C incoming water.

9. Conclusion

The simulation results shown in section 7 provide detailed insight into the processes occurring in a refrigeration system. The results shown in section 8 confirm that the simulation model correlates well with the experimental system; thus the simulation model is successful. The evaporator temperature, LP and HP pressure achieved by the simulation agrees well with the experiment. The heat transfer rates of the evaporator and gas cooler show trends similar to the experiment and reach steady-state values that are close to the experiment.

In conclusion, the transient simulation model of the CO₂ refrigerator runs stably on its own and predicts real life operation fairly accurately; thus, it shows promise in being a valuable tool for designing CO₂ refrigerators if a non-adiabatic transient compressor model is developed.

10. References

- Barthel C., Götz T. 2012. *The overall worldwide saving potential from domestic refrigerators and freezers*. [On-line]. Available: http://www.bigee.net/media/filer_public/2012/12/04/big_ee_doc_2_refrigerators_freezers_worldwide_potential_20121130.pdf [2015, August 7].
- Çengel Y.A., Boles M. A. 2007. *Thermodynamics: An Engineering Approach*. 6 ed. New York: McGraw-Hill.
- Chapra S.C., 2008. *Applied Numerical Methods with MATLAB for Engineers and Scientists*. 2 ed. New York: McGraw-Hill.
- Embraco. [S.a.]. Carbon Dioxide (R744) EK6210CD Compressor Application Manual.
- Fenghour A., Wakeham W.A., Vesovic V. 1998. *The Viscosity of Carbon Dioxide*. J. Phys. Chem. Ref. Data, Vol. 27, No. 1: 31-44.
- Sarkar J. 2009. *Cycle Parameter Optimization of Vortex Tube Expansion Transcritical CO₂ System*. Varanasi: BHU.
- Sarkar J. 2010. *Review on Cycle Modifications of Transcritical CO₂ Refrigeration and Heat Pump Systems*. Varanasi: BHU.
- Scalabrin G., Marchi P., Finezzo F., Span R. 2006. *A Reference Multiparameter Thermal Conductivity Equation for Carbon Dioxide with an Optimized*

Functional Form. J. Phys. Chem. Ref. Data, Vol. 35,
No. 4: 1549-1575.

Span R., Wagner W. 1996. *A New Equation of State for Carbon Dioxide Covering the Fluid Region from the Triple-Point Temperature to 1100 K at Pressures up to 800 MPa.* J. Phys. Chem. Ref. Data, Vol. 25, No. 6: 1509-1596.

Versteeg H.K., Malalasekera W. 2007. *An Introduction to Computational Fluid Dynamics. The Finite Volume Method.* 2 ed. Harlow: Pearson Education Limited.